

AD-A090 424

BALLISTIC RESEARCH LABS ABERDEEN PROVING GROUND MD F/G 20/4
A COMPARISON OF NAVIER-STOKES COMPUTATIONS WITH EXPERIMENTAL DA--ETC(U)
JUN 80 C J NIETUBICZ, L D KAYSER

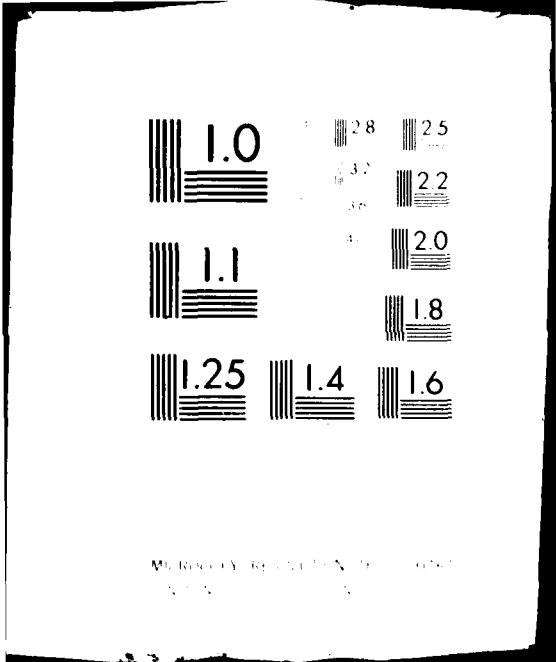
UNCLASSIFIED

NL

/ OF /

AD-A
980424

END
DATE
FILMED
11-80
DTIC



MURPHY RESOLUTION TEST CHART
1951-A

AD A090424

NIETUBICZ & KAYSER

A COMPARISON OF NAVIER-STOKES COMPUTATIONS WITH
EXPERIMENTAL DATA FOR A PROJECTILE SHAPÉ AT TRANSONIC VELOCITIES

CHARLES J. NIETUBICZ, Mr. and LYLE D. KAYSER, Mr.
U.S. Army Ballistic Research Laboratory
Aberdeen Proving Ground, Maryland 21005

11 JUN 1978

I. INTRODUCTION

The in flight characteristics of an artillery shell are of major importance to the shell designer, ballisticion and ultimately the artillery field commander whose mission is deployment of timely and accurate fire power. The aerodynamic properties of artillery shell, such as pitching moment, Magnus moment and drag are critical to the stability of shell which in turn significantly affects accuracy and time of flight. The capability to determine the aerodynamics of shell is required over a wide range of flight regimes since, depending on initial launch velocities, artillery shell are subject to subsonic, transonic, and supersonic flight. Projectile aerodynamics over these various flight regimes have been found, in some cases, to change by an order of magnitude. The solution techniques utilized must therefore be capable of computing these changes.

A concentrated theoretical and experimental research program has been ongoing at BRL in order to develop the predictive capabilities required for determining projectile aerodynamics. Supersonic computations using combined inviscid flow field and boundary layer techniques have been developed by Sturek⁽¹⁾, et al., for cone-cylinder and ogive-cylinder configurations. Recent results have been obtained in supersonic flow over a typical boattailed projectile by Schiff and Sturek⁽²⁾ using modern computational techniques for solving the thin-layer Navier-Stokes equations.

DDC FILE COPY

45

DDIC
OCT 20 1980

U.S. GOVERNMENT PRINTING OFFICE: 1975 O 280-100
For purchase by the general public, contact the Superintendent of Documents, Washington, D.C. 20540
Distribution is limited to the following categories:

80 10 17 002

Inviscid transonic computational results have been obtained by Reklis⁽³⁾, et al., for a secant-ogive-cylinder-boattail shape. The inviscid techniques give good results for pitch plane aerodynamic coefficients at small angle of attack. However, this technique lacks the ability to include viscous effects at transonic speeds and thus compute the Magnus effect on projectiles. Techniques which have been applied in supersonic flow for combining inviscid and boundary layer methods have not been fully established for transonic flow. These methods, which have shown good results for ogive-cylinders in supersonic flow at low angle of attack, are not accurate in modeling the severe flow expansion in the vicinity of surface discontinuities such as those that occur at the cylinder-boattail junction.

The solution of the thin-layer Navier-Stokes equations, which allows for the simultaneous computation of the inviscid and viscous regions, eliminates the need for matching two different solutions. Additionally, since all three momentum equations are retained, the ability to compute in regions of separated flow is achieved. This paper describes the governing three-dimensional thin-layer Navier-Stokes equations used for computing flow over projectile shapes at angle of attack. Secondly, the generalized axisymmetric formulation used for computations at $\alpha = 0^\circ$ will be described. A description of the numerical algorithm and results will follow. Experimental and computational results will be presented for a secant-ogive-cylinder-boattail projectile shape at $\alpha = 0^\circ$ and $\alpha = 2^\circ$. Computational results will also be shown for a ring airfoil shape thus demonstrating the general geometry capability of the present numerical scheme.

II. GOVERNING EQUATIONS

The general three-dimensional thin-layer Navier-Stokes equations, used for all cases where $\alpha = 0^\circ$, are described in Section IIa. The thin-layer generalized axisymmetric equations, which are a special case of the 3-D equations, are described in Section IIb.

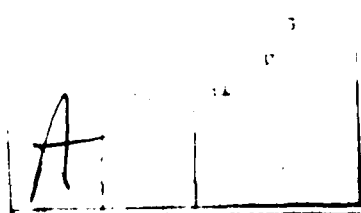
a. Three-Dimensional Equations

The transformed three-dimensional thin-layer Navier-Stokes equations in non-dimensional and strong conservation law form are written as⁽⁴⁾

$$\partial_T \hat{q} + \partial_\xi \hat{E} + \partial_\eta \hat{F} + \partial_\zeta \hat{G} = Re^{-1} \partial_\zeta \hat{S} \quad \left[\begin{array}{l} \text{Adapted from} \\ \text{Ref. 4} \end{array} \right] \quad (1)$$

where general coordinate transformations

446



NIETUBICZ & KAYSER

$\xi = \xi(x,y,z,t)$ - longitudinal coordinate

$\eta = \eta(x,y,z,t)$ - circumferential coordinate

$\zeta = \zeta(x,y,z,t)$ - near Normal coordinate

$\tau = t$ - time

are used and

$$\hat{q} = J^{-1} \begin{bmatrix} \rho \\ \rho u \\ \rho v \\ \rho w \\ e \end{bmatrix} \qquad \hat{E} = J^{-1} \begin{bmatrix} \rho U \\ \rho u U + \xi_x p \\ \rho v U + \xi_y p \\ \rho w U + \xi_z p \\ (e+p)U - \xi_t p \end{bmatrix}$$

$$\hat{F} = J^{-1} \begin{bmatrix} \rho V \\ \rho u V + \eta_x p \\ \rho v V + \eta_y p \\ \rho w V + \eta_z p \\ (e+p)V - \eta_t p \end{bmatrix} \qquad \hat{G} = J^{-1} \begin{bmatrix} \rho W \\ \rho u W + \zeta_x p \\ \rho v W + \zeta_y p \\ \rho w W + \zeta_z p \\ (e+p)W - \zeta_t p \end{bmatrix}$$

$$\hat{S} = J^{-1} \begin{bmatrix} 0 \\ \mu(\zeta_x^2 + \zeta_y^2 + \zeta_z^2)u_\zeta + (\mu/3)(\zeta_x u_\zeta + \zeta_y v_\zeta + \zeta_z w_\zeta)\zeta_x \\ \mu(\zeta_x^2 + \zeta_y^2 + \zeta_z^2)v_\zeta + (\mu/3)(\zeta_x u_\zeta + \zeta_y v_\zeta + \zeta_z w_\zeta)\zeta_y \\ \mu(\zeta_x^2 + \zeta_y^2 + \zeta_z^2)w_\zeta + (\mu/3)(\zeta_x u_\zeta + \zeta_y v_\zeta + \zeta_z w_\zeta)\zeta_z \\ \{(\zeta_x^2 + \zeta_y^2 + \zeta_z^2)[0.5\mu(u^2 + v^2 + w^2)_\zeta + \kappa Pr^{-1}(\gamma-1)^{-1}(a^2)_\zeta] \\ + (\mu/3)(\zeta_x u_\zeta + \zeta_y v_\zeta + \zeta_z w_\zeta)(\zeta_x u_\zeta + \zeta_y v_\zeta + \zeta_z w_\zeta)\} \end{bmatrix}$$

47

The velocities

$$\left. \begin{aligned} U &= \xi_t + \xi_x u + \xi_y v + \xi_z w \\ V &= \eta_t + \eta_x u + \eta_y v + \eta_z w \\ W &= \zeta_t + \zeta_x u + \zeta_y v + \zeta_z w \end{aligned} \right\} \quad (2)$$

represent the contravariant velocity components.

The Cartesian velocity components (u,v,w) are retained as the dependent variables and are nondimensionalized with respect to a_∞ (the free stream speed of sound). The local pressure is determined using the relation

$$p = (\gamma - 1)(e - .5\rho(u^2 + v^2 + w^2)) \quad (3)$$

where γ is the ratio of specific heats, density (ρ), is referenced to ρ_∞ and total energy (e) to $\rho_\infty a_\infty^2$. The additional parameters are (κ) the coefficient of thermal conductivity, (μ) the dynamic viscosity, (Re) the Reynolds number, (Pr) the Prandtl number, and (λ) which through the Stokes hypothesis is $(-2/3)\mu$.

The metric terms ξ_x , η_x and ζ_x are formed from the derivatives x_ξ , y_ξ , z_ξ , etc., and together with the Jacobian of the transformation allow for computations to be performed for variable body geometries.

The "thin-layer" approximation⁽⁴⁻⁷⁾ used here requires that all body surfaces be mapped onto $\zeta = \text{constant}$ planes and that $\text{Re} \gg 1$. Essentially, all the viscous terms in the coordinate directions (here taken as ξ and η) along the body surface are neglected while terms in the ζ or the near normal direction to the body are retained. This approximation is used because, due to computer speed and storage limitations, fine grid spacing can only be provided in one coordinate direction (usually taken as the near normal direction) and the grid spacing available in the other two directions is usually too coarse to resolve the viscous terms. For the type of problems currently under investigation, i.e., projectiles at low angles of attack, with no strong cross-flow separation, these approximations are considered valid.

b. Generalized Axisymmetric Equations

The thin-layer generalized-axisymmetric equations are obtained from the three-dimensional equations by making use of two restrictions: (1) all body geometries are of an axisymmetric type; (2) the state

variables and the contravariant velocities do not vary in the circumferential direction. In what follows, the $\partial_{\eta} \hat{F}$ term of Eq. (1) shall be reduced to the source term of the generalized axisymmetric equations.

A sketch of a typical axisymmetric body is shown in Figure 1a.

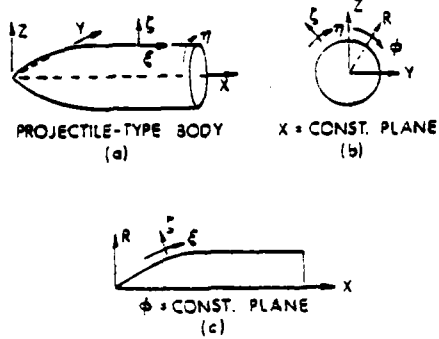


FIGURE 1. AXISYMMETRIC BODY AND COORDINATE SYSTEM

In order to determine the circumferential variation of typical flow and geometric parameters, we first establish correspondence between the inertial Cartesian coordinates (x,y,z) (to which the dependent variables are referenced), the natural inertial cylindrical coordinates (x,phi,R), and the transformed variables (xi,eta,zeta). The choice of the independent variables xi, eta, zeta is restricted, as shown in Figure 1c, insofar as eta must vary as phi, i.e., phi = Ceta (where C is a constant). From the views shown in Figure 1, the relationship between the

coordinate systems are observed to be

$$\left. \begin{aligned} \phi &= C\eta \\ x &= x(\xi, \zeta, \tau) \\ y &= R(\xi, \zeta, \tau) \sin \phi \\ z &= R(\xi, \zeta, \tau) \cos \phi \end{aligned} \right\} \quad (4)$$

where $\phi = \phi(\tau)$ and the Cartesian and cylindrical coordinates are related in the usual way. Note that x and R are general functions of only xi, zeta, and tau.

Evaluating the metric terms given the above assumptions and substituting in Equation (1) the resulting thin-layer generalized axisymmetric equations⁽⁵⁾ can be written as

$$\delta_{\tau} \hat{q} + \delta_{\xi} \hat{E} + \partial_{\zeta} \hat{G} + \hat{H} = Re^{-1} \partial_{\zeta} \hat{S} \quad (5)$$

where

$$\hat{H} = J^{-1} \phi_{\eta} \begin{bmatrix} 0 \\ 0 \\ \rho V [R_{\xi} (U - \xi_t) + R_{\zeta} (W - \zeta_t)] \\ -\rho V R \phi_{\eta} (V - \eta_t) - p / (R \phi_{\eta}) \\ 0 \end{bmatrix} \quad (6)$$

is the resultant source term which has replaced $\partial_{\eta} \hat{F}$ of Equation (1)

Equation (5) contains only two spatial derivatives but does retain all three momentum equations thus allowing a degree of generality over the standard axisymmetric equations. In particular, the circumferential velocity is not assumed to be zero allowing then computations for spinning projectiles or swirl flow to be accomplished.

The numerical algorithm used for both equations (1) and (5) is a fully implicit, approximately factored finite difference scheme as analyzed by Beam and Warming⁽⁸⁾. The algorithm for Equation (1) written in the delta form is

$$\begin{aligned} & (I + h \delta_{\xi} \hat{A}^n - \epsilon_I J^{-1} \nabla_{\xi} \nabla_{\xi} J) (I + h \delta_{\eta} \hat{B}^n - \epsilon_I J^{-1} \nabla_{\eta} \nabla_{\eta} J) x \\ & (I + h \delta_{\zeta} \hat{C}^n - h \text{Re}^{-1} \delta_{\zeta} J^{-1} \hat{M}^n J \epsilon_I J^{-1} \nabla_{\zeta} \nabla_{\zeta} J) (q^{n+1} - q^n) \\ & = -\Delta t (\delta_{\xi} \hat{E}^n + \delta_{\eta} \hat{F}^n + \delta_{\zeta} \hat{G}^n - \text{Re}^{-1} \delta_{\zeta} \hat{S}^n) \\ & \quad - \epsilon_E J^{-1} [(\nabla_{\xi} \nabla_{\xi})^2 + (\nabla_{\eta} \nabla_{\eta})^2 + (\nabla_{\zeta} \nabla_{\zeta})^2] J q^n \end{aligned} \quad (7)$$

where the δ 's are central difference operators, Δ and ∇ are forward or backward difference operators; $h = \Delta t$ corresponds to Euler implicit first-order and $h = \Delta t/2$ to trapezoidal second-order time accuracy. The scheme can be first or second order accurate in time and second or fourth order accurate in space. A similar algorithm can be written for Equation (5) as

NIETUBICZ & KAYSER

$$\begin{aligned}
 & (I + h\delta_{\xi}\hat{A}^n - \epsilon_I J^{-1} \nabla_{\xi} \nabla_{\xi} J) (I + h\delta_{\zeta}\hat{C}^n - \epsilon_I J^{-1} \nabla_{\zeta} \nabla_{\zeta} J) \\
 & - hRe^{-1} \delta_{\zeta} J^{-1} \hat{M}^n J) \times (\hat{q}^{n+1} - \hat{q}^n) = -\Delta t (\delta_{\xi} \hat{E}^n + \delta_{\zeta} \hat{G}^n) \quad (8) \\
 & - Re^{-1} \delta_{\zeta} \hat{S}^n) - \Delta t \hat{H}^n - \epsilon_E J^{-1} [(\nabla_{\xi} \nabla_{\xi})^2] J \hat{q}^n
 \end{aligned}$$

Notice that the second factored terms of Equation (7) has been reduced to the term $\Delta t \hat{H}^n$ and appears on the right hand side of Equation (8). The details of the numerical method, algorithm and boundary conditions for each formulation can be found in References (4) and (5) respectively.

III. MODEL GEOMETRY AND EXPERIMENTAL MEASUREMENTS

The ogive-cylinder boattail shape used for this study closely resembles a modern low-drag artillery projectile and can be seen in the pressure coefficient plot of Figure 2. The model has a three caliber ogive, a two caliber cylinder, and a one caliber 7-degree boattail; the model length is 343mm and the diameter is 57.2mm.

Several wind tunnel experiments have been conducted for this model geometry in order to obtain data for comparison to numerical computations. Experimental data used for comparison in this study are boundary layer profile measurements obtained at the Naval Surface Weapons Center (NSWC), White Oak Laboratory and surface pressure measurements obtained at the NASA Langley Research Center.

Boundary layer data were obtained in the NSWC Tunnel No. 2 which has an open jet test section with a nozzle exit size of 40.6×40.6 cm. Data were acquired at Mach = 0.908 with a supply pressure of one atmosphere and a supply temperature of approximately 320°K; these conditions give a Reynolds number of 4.5×10^6 based on model length. The NSWC Laser Velocimeter used to measure the boundary layer velocities is commonly referred to as a forward scatter, differential Doppler or "fringe" system and is described in Reference (9). Previous boundary layer measurements at Mach = 3.0 obtained by both laser velocimeter and by impact probe measurements showed good agreement. The present Mach = 0.908 profiles, however were not as consistently smooth and uniform as the Mach 3 profiles described in Reference (10).

Surface pressure measurements were obtained in the NASA Langley 8 ft Pressure Tunnel with supply pressures and temperatures of one atmosphere and 320°K respectively. The model was instrumented with pressure taps at 15 longitudinal stations. Data were acquired at Mach numbers of 0.91 to 1.20, angles of attack from 0 to 10 degrees, and for circumferential positions by rolling the model in 22.5 degree increments.

IV. COMPARISONS BETWEEN COMPUTATION AND EXPERIMENT

Computations have been obtained on the same secant-ogive-cylinder-boattail (SOCBT) shape used for the experiment. The 3-D Navier-Stokes equations were used for $\alpha > 0^\circ$ and the generalized axisymmetric formulation for $\alpha = 0^\circ$. Computational results have been obtained for a ring airfoil shape which show an interesting shock pattern being developed as a function of Mach number.

a. Secant-Ogive-Cylinder-Boattail, $\alpha = 0^\circ$

A computational finite difference mesh of 78 longitudinal points by 50 normal points were used for these calculations. For the experimental test condition of Mach = 0.908 the surface pressure coefficient, C_p is shown as a function of axial position in Figure 2.

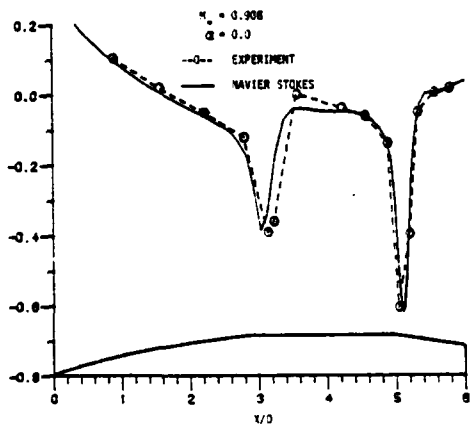


FIGURE 2. EXPERIMENTAL AND THEORETICAL COMPARISON OF SURFACE PRESSURE COEFFICIENT FOR SOCBT, $M = 0.908$

The computational results, indicated by the solid line are shown to be in good agreement with the experimental results. The flow expansion (decrease in C_p) and subsequent shock (increase in C_p) can be seen occurring near the nose-cylinder and cylinder-boattail junctions. An accurate computation of the pressure distribution is important since it is the integration of surface pressures which are primarily used to determine the aerodynamic coefficients.

Increasing the Mach number to $M = 0.96$ (Figure 3) shows the movement of shock position, which is typical of transonic flow. Again the experiment and computations show good agreement with the exception of the boattail region. This discrepancy is attributed to

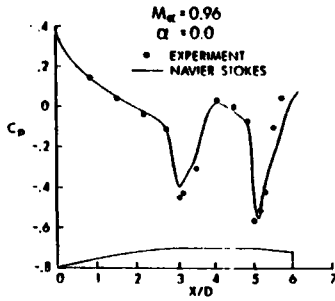


FIGURE 3. EXPERIMENTAL AND THEORETICAL COMPARISON OF SURFACE PRESSURE COEFFICIENT FOR SOCBT, $M = .96$

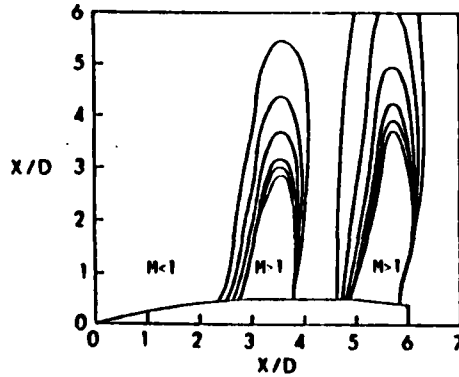


FIGURE 4. MACH CONTOURS AT $M = .96$ FOR SOCBT, $\alpha = 0.0$

inadequate grid resolution in the vicinity of the shock. A more detailed look at the computed shock position can be seen in Figure 4 (above) where Mach contours have been plotted. The coalescence of the Mach lines represent the position of the shock and regions of subsonic and supersonic flow are identified.

The accurate determination of aerodynamic coefficients is extremely important throughout the transonic regime since the magnitude of the coefficients can change by as much as 100% in this area. A series of computations were obtained from $M = 0.8$ through $M = 1.1$ and the surface pressures were integrated to determine the aerodynamic wave drag. The results are shown in Figure 5 together with the experimental data. Excellent agreement is shown for both the drag rise and magnitude of the zero yaw drag, C_{D0} , in the critical Mach number regime.

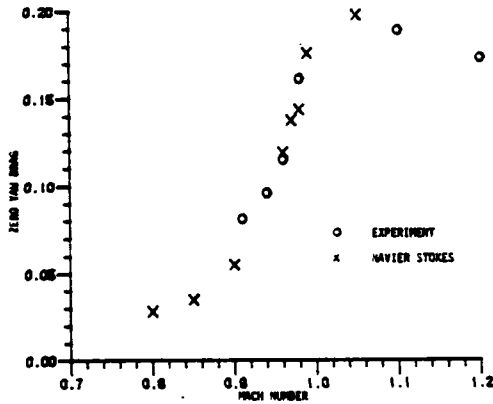


FIGURE 5. ZERO YAW DRAG FOR SOCBT, $\alpha = 0$. THEORY AND EXPERIMENT.

The dynamic stability of shell is one area of concern when designing new shell or modifying existing ones. The Magnus moment, which affects the dynamic stability, is a viscous phenomena. Therefore an accurate representation of the viscous portion of the flow field is crucial to computing the Magnus moment. As an initial attempt to look at the boundary layer in transonic flow, with its associated shock interaction, computations were performed at $M = 0.908$, $\alpha = 0^\circ$ and comparison of computational velocity profiles with experimental profiles were made; an example of this comparison is shown in Figure 6. The

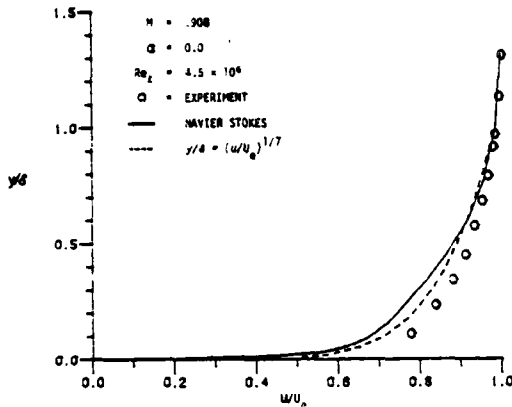


FIGURE 6. VELOCITY PROFILES AT $x/D = 4.54$

Navier-Stokes result is the solid line and the circles are the experimental results. Although the computational and experimental velocity profiles are not in particularly good agreement, the shape of the computed profiles is seen to be characteristic of a turbulent boundary layer. A power law velocity profile, characteristic of turbulent flow, is included for comparison.

b. Secant-Ogive Cylinder Boattail, $\alpha = 2^\circ$

A new finite difference mesh consisting of 60 longitudinal points, 28 normal points and 20 points in the circumferential direction was designed for computations at angle of attack. Clustering of the longitudinal points was maintained in the vicinity of the expansion similar to the $\alpha = 0^\circ$ cases. The computed leeward ($\phi = 0^\circ$) surface pressure coefficients, as a function of longitudinal position are shown in Figure 7 compared to the experimental results. The computed results are shown to follow the same trend as the experimental data. The agreement in the vicinity of both expansions is quite good but falls off on the cylinder and boattail. A major problem in running 3-D computations is the large number of grid points required for adequate resolution. Increasing the number of longitudinal points, similar to the amount used for $\alpha = 0^\circ$ (78 points) should result in better agreement.

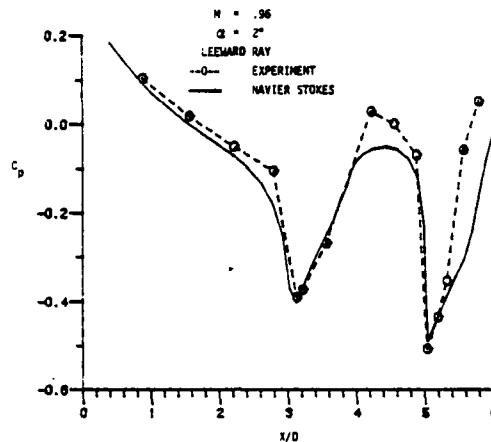


FIGURE 7. COMPARISON OF EXPERIMENTAL AND COMPUTATIONAL SURFACE PRESSURE COEFFICIENTS FOR SOCAT. $\alpha = 2^\circ$

c. Hollow Projectile, $\alpha = 0^\circ$

Of current interest in shell design is the utilization of hollow projectiles which have the characteristic of "flat" trajectories. A shape of this type, known as the ring airfoil, has been type classified and is currently used as an anti riot device. In order to demonstrate the general geometry capabilities of the Navier-Stokes codes, computations were performed for a ring airfoil shape at $\alpha = 0^\circ$. A cross section of the actual shape is shown at the bottom of the C_p plot of Figure 8a. Inviscid results are presented in Figures 8a, b, c and d for $M = 0.4, 0.7, 0.8$ and 0.9 . In all cases the pressure distribution is plotted for the internal and external surfaces using a solid line and dashed line respectively.

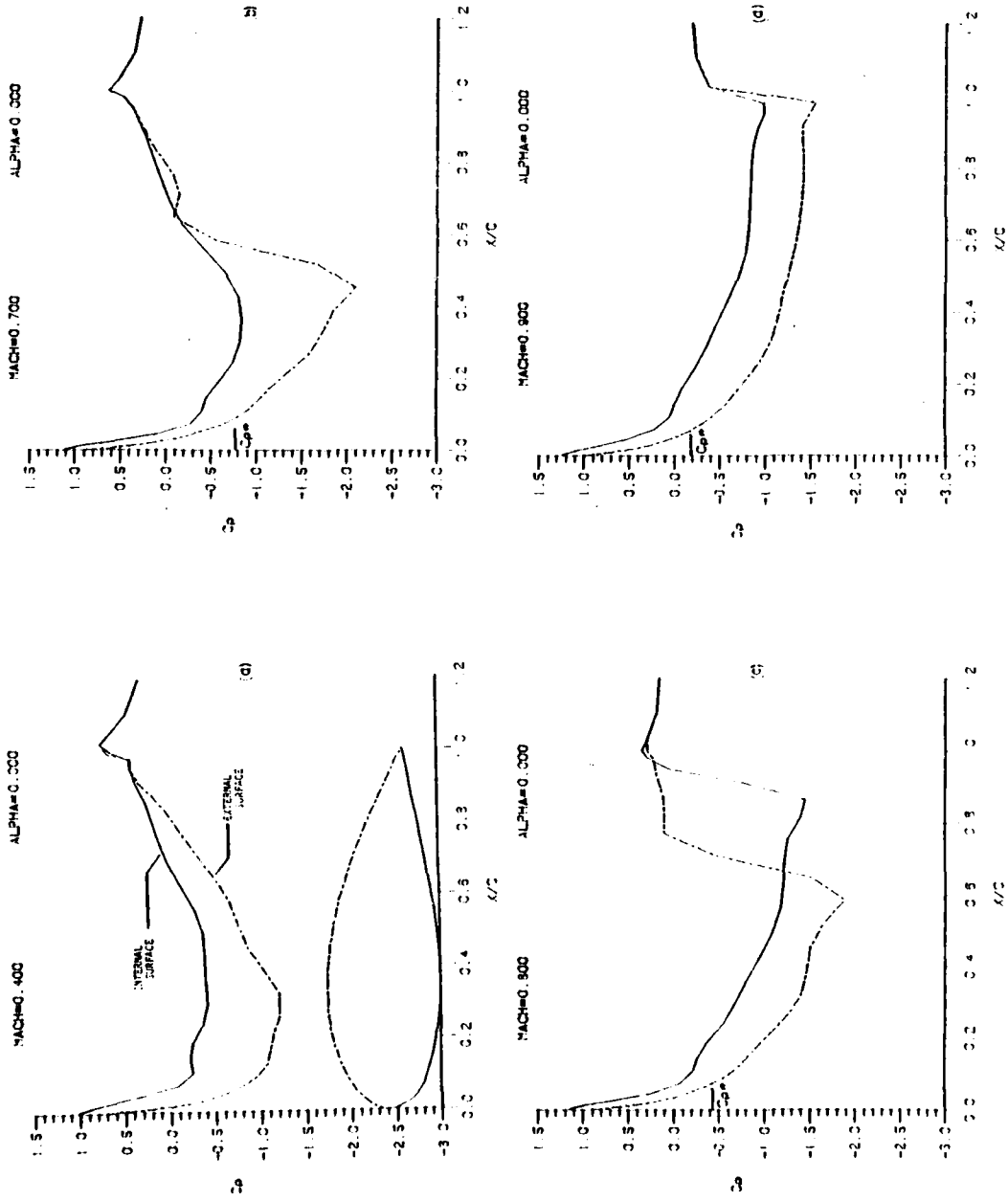


FIGURE 8. INVISCID TRANSONIC FLOW OVER A RING AIRFOIL PROJECTILE, $M = .4$ THRU $M = .9$

(56)

The critical pressure coefficient, C_p^* , is the value of the pressure coefficient at sonic velocity. The flow velocity in regions with pressure greater than C_p^* is subsonic and in regions where the pressure is less than C_p^* the flow is supersonic. For $M = 0.4$ (Figure 8a), all values of C_p are greater than C_p^* indicating the flow over both the internal and external surfaces is subsonic. However, as the Mach number is increased to 0.7, the upper surface is shown to develop supersonic flow and a shock wave while the internal flow remains subsonic. Increasing the Mach number still further to $M = 0.8$, the shock waves are now seen to exist on both the external and internal surfaces. A final solution at $M = 0.9$ shows that the shock wave has moved to the trailing edge indicating supersonic flow over most of the internal and external surfaces.

V. SUMMARY

Implicit finite difference methods have been used to solve the thin-layer Navier-Stokes equations. Both the three-dimensional and generalized axisymmetric equations have been presented and solutions of the flow field about projectile shapes have been obtained.

The computed surface pressure coefficients on the ogive-cylinder-boattail projectile were found to be in excellent agreement with the experimental data for $\alpha = 0^\circ$. The generalized axisymmetric equations used for these computations are similar to the 2-D equations and thus have no severe limitation on the number of mesh points required for a good solution.

Computations for the same projectile shape at $\alpha = 2^\circ$, using the 3-D equations, show good agreement with the experimental data. Computational experimentation indicate that improved agreement could be obtained with increased grid resolution.

Computations of the viscous boundary layer indicate the correct trend for a turbulent velocity profile which is critical to the determination of Magnus moment. Additional experimental velocity profiles are required to fully assess the accuracy of the Navier-Stokes computations in the viscous region.

The general geometry capability of the numerical scheme was demonstrated by solving the inviscid flow field about a ring airfoil projectile. The ability to compute in regions of pure subsonic flow and mixed subsonic/supersonic flow has been demonstrated.

NIETUBICZ & KAYSER

REFERENCES

1. W. B. Sturek, et al., "Computations of Magnus Effects for a Yawed, Spinning Body of Revolution", AIAA Journal, Vol. 16, No. 7, July 1978, pp. 687-692.
2. L. B. Schiff and W. B. Sturek, "Numerical Simulation of Steady Supersonic Flow Over Cone Ogive-Cylinder-Boattail Body, AIAA Paper No. 80-0066, January 14-16, 1980.
3. R. P. Reklis, W. B. Sturek and F. L. Bailey, "Computation of Transonic Flow Past Projectiles at Angle of Attack", U.S. Army ARRADCOM Technical Report, ARBRL-TR-02139, February 1979.
4. T. H. Pulliam and J. L. Steger, "On Implicit Finite-Difference Simulations of Three-Dimensional Flow", AIAA Paper No. 78-10, January 1978.
5. C. J. Nietubicz, T. H. Pulliam and J. L. Steger, "Numerical Solution of the Azimuthal-Invariant Thin-Layer Navier-Stokes Equations", AIAA Paper No. 79-0010, January 1979.
6. J. L. Steger, "Implicit Finite Difference Simulation of Flow About Arbitrary Geometries With Application to Airfoils", AIAA Paper No. 77-665, June 1977.
7. B. S. Baldwin and H. Lomax, "Thin Layer Approximation and Algebraic Model for Separated Turbulent Flows", AIAA Paper No. 78-257, January 1978.
8. R. Beam and R. F. Warming, "An Implicit Factored Scheme for the Compressible Navier-Stokes Equations", AIAA Paper No. 77-645, June 1977.
9. W. J. Yanta and R. E. Lee, "Measurements of Mach 3 Turbulence Transport Properties on a Nozzle Wall", AIAA Journal, Vol. 14, No. 6, June 1976, pp. 725-729.
10. L. D. Kayser, W. J. Yanta and W. B. Sturek, "Measurements in the Turbulent Boundary Layer of a Yawed, Spinning Body of Revolution at Mach 3.0 with a Laser Velocimeter and Impact Probe", U.S. Army ARRADCOM Technical Report, ARBRL-TR-02074, May 1978.